



Modal decomposition of fluid–structure interaction with application to flag flapping

Andres Goza ^{a,*}, Tim Colonius ^b

^a Department of Mechanical and Aerospace Engineering, Princeton University, Princeton, NJ 08540, USA

^b Division of Engineering and Applied Science, California Institute of Technology, Pasadena, CA 91125, USA



ARTICLE INFO

Article history:

Received 13 February 2018

Received in revised form 14 June 2018

Accepted 25 June 2018

Keywords:

Fluid–structure interaction

Modal decomposition

Proper orthogonal decomposition

Dynamic mode decomposition

ABSTRACT

Modal decompositions such as proper orthogonal decomposition (POD), dynamic mode decomposition (DMD) and their variants are regularly used to deduce physical mechanisms of nonlinear flow phenomena that cannot be easily understood through direct inspection. In fluid–structure interaction (FSI) systems, fluid motion is coupled to vibration and/or deformation of an immersed structure. Despite this coupling, data analysis is often performed using only fluid or structure variables, rather than incorporating both. This approach does not provide information about the manner in which fluid and structure modes are correlated. We present a framework for performing POD and DMD where the fluid and structure are treated together. As part of this framework, we introduce a physically meaningful norm for FSI systems. We first use this combined fluid–structure formulation to identify correlated flow features and structural motions in limit-cycle flag flapping. We then investigate the transition from limit-cycle flapping to chaotic flapping, which can be initiated by increasing the flag mass. Our modal decomposition reveals that at the onset of chaos, the dominant flapping motion increases in amplitude and leads to a bluff-body wake instability. This new bluff-body mode interacts triadically with the dominant flapping motion to produce flapping at the non-integer harmonic frequencies previously reported by Connell and Yue (2007). While our formulation is presented for POD and DMD, there are natural extensions to other data-analysis techniques.

© 2018 Elsevier Ltd. All rights reserved.

1. Introduction

Modal decompositions such as proper orthogonal decomposition (POD) and dynamic mode decomposition (DMD) have been used to distill important physical mechanisms from data and to develop reduced-order models for turbulent wall-bounded flows (Berkooz et al., 1993), flow past a cylinder (Chen et al., 2012; Bagheri, 2013), and a jet in cross-flow (Rowley et al., 2009; Schmid, 2010), to name a few examples.

These techniques were developed for flows involving (at most) stationary immersed surfaces, and have been applied less extensively to fluid–structure interaction (FSI) problems, where the fluid motion is coupled to deformation and/or vibration of an immersed structure. In this FSI setting, data analysis has, to our knowledge, only been applied to data of either the fluid or the structure independently of the other. The fluid-only approach has been used to study flow past a flexible membrane (Schmid, 2010), a cantilevered beam (Cesur et al., 2014), and an elastically-mounted cylinder undergoing vortex-induced vibration (Blanchard et al., 2017). The solid-only approach has been applied to fish swimming (Bozkurttas et al., 2009;

* Corresponding author.

E-mail address: ajgoza@gmail.com (A. Goza).

Tangorra et al., 2010) and flag flapping (Michelin et al., 2008; Kim et al., 2013). These approaches reveal significant flow or structure behavior, respectively, but do not yield driving mechanisms in the omitted quantity. This in turn leaves the correlation between fluid and structure behavior unknown.

We propose a framework for data analysis of FSI systems where the fluid and structure are treated together, which naturally allows correlation between the fluid and structure to inform the resulting modes of the fully-coupled system. As part of this formulation, we define a norm in terms of the total mechanical energy of the FSI system. This combined fluid–structure data-analysis procedure is then demonstrated on limit-cycle flapping and chaotic flapping of strictly two-dimensional flags.

In the case of chaotic flapping, previous work identified that for flags of low stiffness, chaos can be triggered by increasing the flag mass (Connell and Yue, 2007; Alben and Shelley, 2008). For flows at moderate Reynolds numbers of $O(1000)$, Connell and Yue (2007) showed that the flag system transitions with increasing mass from a stable equilibrium to limit-cycle flapping of increasing amplitude, then to chaotic flapping. Alben and Shelley (2008) found similar transitions in inviscid fluids. In the viscous case, the transition to chaos is associated with the appearance of a distinct frequency that is a noninteger harmonic of the dominant flapping frequency (Connell and Yue, 2007), though the cause of this new frequency signature is as yet unexplained. We use our coupled FSI decomposition to identify the mechanism responsible for the appearance of this noninteger frequency harmonic.

We focus here on proper orthogonal decomposition (POD) and dynamic mode decomposition (DMD) because of their widespread use and their expected suitability for the problems considered here. The limit-cycle case described in Section 3.1 is associated with one dominant frequency, and thus DMD is a natural candidate because of its localized harmonic nature (Mezić, 2013). POD is also expected to be suitable because of the near-harmonic decomposition it typically yields for limit-cycle flows (such as occurs in vortex shedding past a cylinder near the critical Reynolds number of approximately 47; see, e.g., Kutz et al., 2016). For the chaotic flapping problem described in Section 3.2, the non-broadband ('peaky') nature of the dynamics again makes DMD a fitting technique. However, POD and DMD are not ideal for all contexts. For example, Towne et al. (2018) demonstrated that in statistically stationary flows with broadband frequency content — as observed in the majority of turbulent flows — spectral POD provides an optimal decomposition. The major goal of the current work is to demonstrate the utility of performing data analysis in a manner that accounts for both the fluid and the structure, rather than explore the advantages of any particular technique, a question which in any event depends on the specific FSI problem under consideration. Future work can readily incorporate the methodology presented here into the appropriate technique for the intended application.

2. POD and DMD of fluid–structure interaction

We consider snapshot-based methods applied to discrete data. The associated data matrices are assumed to be organized so that each column provides the state of the system at an instance in time and each row contains the time history of a specific state variable. For simplicity, the formulation is presented in a two-dimensional setting; the extension to three dimensions is straightforward.

We assume fluid data is given on a stationary Cartesian grid, Ω , made up of n_f points ($\Omega \subset \mathbb{R}^{1 \times n_f}$), and let the streamwise and transverse fluid velocities at the i th time instance, t_i , be $\mathbf{u}_i, \mathbf{v}_i \in \Omega$. Fluid data is often provided in this format by immersed-boundary methods and experiments; some numerical methods use moving meshes at each time step that conform to the moving structure, and fluid data obtained from these methods would need to be interpolated onto a single stationary grid at each time instance to use the method we propose here.

We consider structural data provided in a Lagrangian setting, with the structural domain, Γ , comprised of n_s points ($\Gamma \subset \mathbb{R}^{1 \times n_s}$ depends on time). We let $\chi_i, \eta_i \in \Gamma$ denote the streamwise and transverse structural displacements from an undeformed reference configuration at the i th time instance, and $\xi_i, \zeta_i \in \Gamma$ be the corresponding structural velocities. We define the total state vector at t_i as $\mathbf{y}_i = [\mathbf{u}_i, \mathbf{v}_i, \chi_i, \eta_i, \xi_i, \zeta_i]^T \in \mathbb{R}^{2n_f + 4n_s}$, and define the data matrix, $\mathbf{Y} \in \mathbb{R}^{n \times m}$ ($n = 2n_f + 4n_s$ is the size of the state and m is the number of snapshots), as $\mathbf{Y} = [\mathbf{y}_1, \dots, \mathbf{y}_m]$.

POD modes are computed from the mean-subtracted data matrix, $\tilde{\mathbf{Y}}$, whose i th column is defined as $\tilde{\mathbf{y}}_i = \mathbf{y}_i - \boldsymbol{\mu}$, where $\boldsymbol{\mu} = 1/m \sum_{k=1}^m \mathbf{y}_k$ is the sample temporal mean of \mathbf{Y} . For DMD, Chen et al. (2012) found that the use of $\tilde{\mathbf{Y}}$ reduces DMD to a discrete Fourier transform in time, and that using \mathbf{Y} allows for growth-rate information to be retained. For this reason, DMD is performed on \mathbf{Y} below.

The immersed structure is assumed to be thin in the ensuing discussion, as occurs for problems involving flags, bio-inspired wings and fins, spring-mounted flat plates, etc. For bodies of non-negligible thickness, points on Ω lie within the immersed body at any time instance, leading to spurious contributions from the 'fictitious fluid' within $\Omega \cap \Gamma$. Addressing this challenge is a subject of future work.

2.1. Proper orthogonal decomposition

POD decomposes the data into orthogonal spatially uncorrelated modes that are ordered such that the leading k modes ($k \leq m$) provide the most energetically dominant rank- k representation of $\tilde{\mathbf{Y}}$. This optimal representation is defined with respect to a norm, and we therefore select an inner product space whose induced norm yields the mechanical energy of the FSI system. We first motivate this choice of norm within a continuous-variable setting, and subsequently provide details

of the norm in the discrete setting relevant for data. Defining \mathbf{x} as an Eulerian spatial coordinate and $\tilde{\mathbf{x}}$ as a Lagrangian coordinate marking the material points in a reference configuration (typically the undeformed state), and letting $\mathbf{u}(\mathbf{x}, t) = [u(\mathbf{x}, t), v(\mathbf{x}, t)]^T$, $\chi(\tilde{\mathbf{x}}, t) = [\chi(\tilde{\mathbf{x}}, t), \eta(\tilde{\mathbf{x}}, t)]^T$, $\xi(\tilde{\mathbf{x}}, t) = [\xi(\tilde{\mathbf{x}}, t), \zeta(\tilde{\mathbf{x}}, t)]^T$, Ω and Γ be continuous analogues of the discrete variables defined earlier, the mechanical energy is

$$E(t) = \frac{\rho_f}{2} \int_{\Omega} |\mathbf{u}|^2 d\Omega + \int_{\Gamma} \left[\kappa(\chi) + \frac{\rho_s}{2} |\xi|^2 \right] d\Gamma. \quad (1)$$

The terms corresponding to the fluid and structural velocities represent the kinetic energy in the system (ρ_f and ρ_s are the fluid and structure density, respectively) and $\kappa(\chi)$ is the potential (strain) energy within the structure.

The potential energy, κ , is in general a material-dependent nonlinear nonnegative function of the deformation gradient of the structure (Bathe, 2014), but has an intuitive expression for several practical cases. For example, $\kappa = k\chi^2/2$ for a spring-mounted rigid body, where k is the spring constant and in this context χ refers to the deflection of the spring from its neutral position. In the more general case of a hyperelastic isotropic material that obeys a linear stress–strain relation (Bathe, 2014),

$$\kappa = \frac{\lambda}{2} [\text{trace}(\mathbf{E})]^2 + G[\text{trace}(\mathbf{E}^2)] + \tilde{\kappa} \quad (2)$$

where λ and G are the Lamé constants, $E_{ij} = 1/2(\partial\chi_i/\partial\tilde{x}_j + \partial\chi_j/\partial\tilde{x}_i + \partial\chi_i/\partial\tilde{x}_j\partial\chi_j/\partial\tilde{x}_i)$ is the Green-Lagrangian strain tensor, and $\tilde{\kappa}$ is the pre-strain associated with the reference configuration (in most cases, the reference configuration is the undeformed state and $\tilde{\kappa} = 0$). Note that the use of \mathbf{E} allows for treatment of problems undergoing large displacements, rotations, and strains, so long as the material is isotropic and the stress–strain relationship is linear. In the flag-flapping problems of interest here, the bending strain can be expressed using (2); moreover, it is typical in these problems for displacements to be large but strains to be small, in which case the quadratic terms in \mathbf{E} may be neglected.

The mechanical energy is a natural choice for defining the norm: for many structures (including elastically-mounted bodies and hyperelastic materials with strain energies of the form (2)), and under the assumption that there are no body forces and that the shear stress is negligible on the boundary of Ω (which occurs for sufficiently large Ω),

$$\frac{dE(t)}{dt} = -2\mu \int_{\Omega} (\nabla\mathbf{u} + (\nabla\mathbf{u})^T) : (\nabla\mathbf{u} + (\nabla\mathbf{u})^T) d\Omega \leq 0 \quad (3)$$

where μ is the dynamic viscosity of the fluid. Note that we assumed no dissipation in the structure in arriving at (3). Including this term would modify (3) by a term that depends on the properties of the structure but in any case is nonpositive. In deriving (3) it is most convenient to reformulate the integration over Γ as an integration over the reference configuration (say, Γ_0). This allows for (2) to be used directly (since \mathbf{E} is defined with respect to the reference configuration), and avoids the use of Leibniz's rule when taking the time derivative (since Γ_0 does not change in time). Eq. (3) has a physical interpretation: as the system progresses in time, energy is exchanged between the kinetic energy of the flow, kinetic energy of the structure, potential (bending strain) energy in the structure, and viscous dissipation in the fluid. The mechanical energy accounts for all of these exchanges except for viscous dissipation, which only acts to reduce the system energy.

While the mechanical energy is a physically intuitive choice of norm, there are other possibilities (so long as so the result is an induced norm of an inner-product space). For example, one option is to give different weights to the various terms in (1) depending on what behavior is expected to dominate for a given system. One limiting case is to set the structural terms to zero, so that the flow dictates the decomposition. We restrict ourselves to the mechanical energy in the present work, though future studies could investigate the effect of various weights on the optimality of the modal decomposition for a given problem.

Returning to the discrete setting within which data is collected, the norm based on the mechanical energy of the FSI system may be written as $\|(\cdot)\|_{\mathbf{W}} \equiv \|\mathbf{W}(\cdot)\|_2$, where \mathbf{W} is a weighting matrix defined as

$$\mathbf{W} = \begin{bmatrix} \beta_f \mathbf{I}^{2n_f} & \mathbf{0} & \mathbf{0} \\ \mathbf{0} & \beta_{\kappa} \mathbf{L} & \mathbf{0} \\ \mathbf{0} & \mathbf{0} & \beta_s \mathbf{I}^{2n_s} \end{bmatrix}. \quad (4)$$

In this expression, \mathbf{I}^n is the $n \times n$ identity matrix; $\mathbf{L} \in \mathbb{R}^{2n_s \times 2n_s}$ is constructed so that $\tau^T \mathbf{L} \tau$ is an approximation of κ , where $\tau = [\chi, \eta]^T$; and β_f , β_{κ} , and β_s are constants that incorporate the relevant physical parameters and scaling to approximate the integration involved in (1) (e.g., $\beta_f = \Delta x \sqrt{\rho_f}/2$ assuming that the flow grid spacing is uniform; unequal spacings can be incorporated in the standard ways). The specific form of \mathbf{W} for the flag-flapping problem considered here is described in Appendix.

The inner product associated with this weighting matrix is defined as $\langle \mathbf{q}, \mathbf{p} \rangle_{\mathbf{W}} \equiv \mathbf{q}^T \mathbf{W}^T \mathbf{W} \mathbf{p} = (\mathbf{W} \mathbf{q})^T (\mathbf{W} \mathbf{p}) \forall \mathbf{q}, \mathbf{p} \in \mathbb{R}^n$ and the induced norm is $\|\mathbf{q}\|_{\mathbf{W}} \equiv \sqrt{\langle \mathbf{q}, \mathbf{q} \rangle_{\mathbf{W}}} = \sqrt{(\mathbf{W} \mathbf{q})^T (\mathbf{W} \mathbf{q})} \forall \mathbf{q} \in \mathbb{R}^n$, which is a discrete approximation of the square root of (1).

The energetically ordered POD modes with respect to the \mathbf{W} -weighted norm may be written in terms of the singular value decomposition (SVD) $\mathbf{W} \tilde{\mathbf{Y}} = \mathbf{U} \Sigma \mathbf{V}^T$, where Σ is a diagonal matrix containing the singular values $\sigma_1, \dots, \sigma_m$ ordered by decreasing energy, and \mathbf{U} (\mathbf{V}) has columns \mathbf{u}_j (\mathbf{v}_j) containing the left (right) singular vectors that correspond to σ_j . In this notation, the POD modes are $\hat{\mathbf{U}} \equiv \mathbf{W}^{-1} \mathbf{U}$ (note that they are orthogonal with respect to the \mathbf{W} -weighted inner product).

These modes are written in terms of the SVD, but may be computed more efficiently using the method of snapshots (Sirovich and Kirby, 1987). The energetically optimal rank- k ($k \leq m$) approximation of a snapshot \mathbf{y}_i may be expressed through an orthogonal projection onto the POD modes as

$$\mathbf{y}_i \approx \sum_{j=1}^k \hat{\mathbf{u}}_j^T (\mathbf{W}\mathbf{y}_i) \hat{\mathbf{u}}_j. \tag{5}$$

2.2. Dynamic mode decomposition

Whereas POD modes define an energetically optimal representation of the data, DMD modes are obtained from a linear regression that best represents the dynamics of a (potentially nonlinear) data set. Though there are more general variants (Tu et al., 2014), we compute DMD modes from the matrix \mathbf{A} that best maps the progression of the state from one time instance to the next; i.e., the \mathbf{A} that satisfies $\min \sum_{j=1}^{m-1} \|\mathbf{y}_{j+1} - \mathbf{A}\mathbf{y}_j\|_2$.¹ This relation can often be satisfied exactly under reasonable conditions on the data (such as linear independence of the columns of \mathbf{Y}), and the best-fit matrix is $\mathbf{A} = \mathbf{Y}'(\mathbf{Y}'')^\#$, where $\mathbf{Y}' = [\mathbf{y}_2, \dots, \mathbf{y}_m]$, $\mathbf{Y}'' = [\mathbf{y}_1, \dots, \mathbf{y}_{m-1}]$, and $(\mathbf{Y}'')^\#$ is the pseudo-inverse of \mathbf{Y}'' .

DMD modes are the eigenvectors of \mathbf{A} , denoted as $\Phi = [\phi_1, \dots, \phi_{m-1}]$. These modes may be computed efficiently without forming \mathbf{A} explicitly (Tu et al., 2014). The corresponding eigenvalues, $\hat{\gamma}_1, \dots, \hat{\gamma}_{m-1}$, are structured such that $\hat{\gamma}_j = e^{2\pi\gamma_j\Delta t}$, where Δt is the time step between two snapshots and γ_j is a complex number whose real and imaginary parts give the growth rate and frequency, respectively, of mode j . Note that γ_j may be computed from $\hat{\gamma}_j$ via $\gamma_j = \log(\hat{\gamma}_j)/(2\pi\Delta t)$. A k th order ($k \leq m - 1$) representation of the system at the i th time instance t_i may be written in terms of the DMD modes as

$$\mathbf{y}_i \approx \sum_{j=1}^k c_j e^{2\pi\gamma_j t_i} \phi_j \tag{6}$$

where $c_j = (\Phi^\# \mathbf{y}_1)_j$ represents the initial condition in terms of the j th DMD mode.

The above describes the DMD formulation derived for flows without bodies or flows involving stationary bodies, and may be used without modification for FSI problems to obtain the coupled flow-structure behavior that best represents the full system dynamics.

2.3. Implications and directions for reduced-order modeling

Regardless of the technique employed, the ultimate aim of data-driven decomposition is often to develop robust and efficient reduced-order models. To this end, the incorporation of our combined fluid–structure formulation into POD and DMD provides a framework for using either projection-based or equation-free models. We note that there are additional conditions that must be considered to successfully incorporate this combined decomposition into low-order models, such as enforcing the inextensibility of the structure (which is not inherent to the decomposition). Addressing these challenges has potential benefits: most current models are derived by performing a data-driven decomposition of the fluid and coupling this to the full governing equations for the structure (see Dowell and Hall, 2001 for a review), and a combined fluid–structure treatment could lead to more efficient representations. This research direction is left as future work.

3. Application to flag flapping

The dynamics of flag flapping are governed by the Reynolds number (Re) and the dimensionless mass (M_ρ) and bending stiffness (K_B), defined as

$$Re = \frac{\rho_f UL}{\mu}, \quad M_\rho = \frac{\rho_s h}{\rho_f L}, \quad K_B = \left(\frac{E}{\rho_f U^2} \right) \left(\frac{I}{L^3} \right) \equiv R_E R_{sh} \tag{7}$$

where ρ_f (ρ_s) is the fluid (structure) density, U is the freestream velocity, L is the flag length, μ is the dynamic viscosity of the fluid, h is the flag thickness, E is Young’s modulus, I is the second moment of area, and R_E and R_I are the normalized Young’s modulus and moment area.

The flag undergoes large displacements and rotations but small strains; i.e., the only structural nonlinearity is geometrical. The bending strains can thus be computed from (2), with the quadratic terms in \mathbf{E} neglected. We take the reference configuration to be the undeformed state (using a deformed configuration only produces an offset, $\tilde{\kappa}$, in the bending strain that we avoid here for simplicity). The Lagrangian coordinates \tilde{x} and \tilde{y} introduced in Section 2.1 are therefore the streamwise and transverse coordinates of the flag in the undeflected position, and $\chi(\tilde{\mathbf{x}})$ and $\eta(\tilde{\mathbf{x}})$ are the corresponding displacements

¹ The minimization can also be performed with respect to the \mathbf{W} -weighted norm, but we retain the use of the standard 2-norm for consistency with most approaches in the literature.

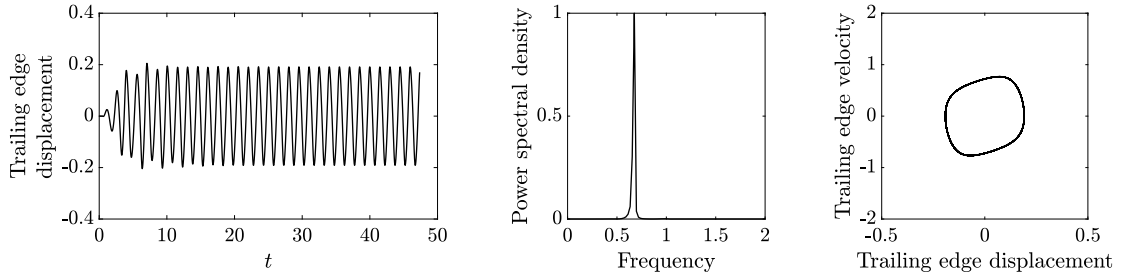


Fig. 1. For limit-cycle flapping with $Re = 500$, $M_\rho = 0.18$, and $K_B = 0.0001$: transverse displacement (left) and spectral density (middle) of the transverse motion of the trailing edge; (right) phase portrait of the transverse velocity versus the transverse displacement of the trailing edge.

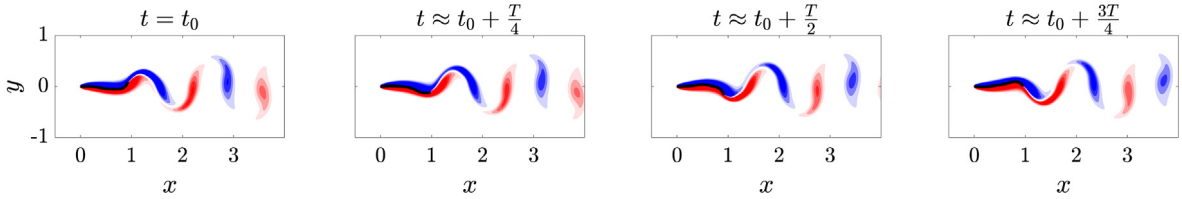


Fig. 2. Snapshots of a flapping period for a flag in limit-cycle flapping with $Re = 500$, $M_\rho = 0.18$, $K_B = 0.0001$. The figure titles indicate the approximation portion of the phase cycle to which the snapshots correspond, with t_0 denoting the time at which the maximal peak displacement occurs. Contours are of vorticity, in 18 increments from -5 to 5 .

from the undeformed configuration. Note that since the flag is thin, $-h \leq \tilde{y} \leq h$ with $h \ll 1$, and thus $\partial(\cdot)/\partial\tilde{y}$ is negligible. Under these simplifications, (2) reduces to

$$\kappa = \frac{1}{2} \left[\left(\frac{R_\lambda}{2} + R_G \right) \left(\frac{\partial \chi}{\partial \tilde{x}} \right)^2 + \frac{R_G}{2} \left(\frac{\partial \eta}{\partial \tilde{x}} \right)^2 \right]. \quad (8)$$

In this expression, R_λ and R_G are the nondimensionalized Lamé parameters. Denoting Poisson's ratio by ν , these parameters may be defined as $R_\lambda = (R_E)(\nu)/((1 + \nu)(1 - 2\nu))$ and $R_G = R_E/(2(1 + \nu))$. The formulation of \mathbf{W} using the dimensionless parameters in (7) and the expression (8) for κ is provided in Appendix.

As a brief aside, the geometric nonlinearity can also be accounted for by moving to a local tangent-normal coordinate system, which is convenient since in this frame the structural motion is governed by a linear Euler Bernoulli equation. Letting \hat{x} and \hat{y} denote the local tangent and normal directions, and $\hat{\chi}$ and $\hat{\eta}$ represent the corresponding displacements, the bending strain may be written as $\kappa = K_B/2(\partial^2 \hat{\eta}/\partial \hat{x}^2)^2$. However, in most cases the displacements are stored in a global coordinate frame with respect to a reference configuration, and the expression (8) must be used instead.

The data for this analysis was obtained using the immersed-boundary method of Goza and Colonius (2017). The method allows for arbitrarily large flag displacements and rotations, and is strongly coupled to account for the nonlinear coupling between the flag and the fluid. The method was validated on several flapping-flag problems (see reference Goza and Colonius, 2017 for details). The physical parameters for each run are described in the subsequent subsections. The simulation parameters used for all cases below are as follows. The flow equations are solved using a multidomain approach, with the finest grid surrounding the body and grids of increasing coarseness used as distance from the body increases (see Colonius and Taira, 2008 for details). The finest domain is of size $[-0.2, 1.8] \times [-0.6, 0.6]$, and the entire flow domain size is $[-15.14, 16.74] \times [-9.536, 9.536]$. The grid spacing on the finest subdomain is $\Delta x = 0.004$, and the time step is $\Delta t = 0.0005$. The immersed-boundary spacing is twice that of the flow grid spacing on the finest sub-domain.

3.1. Limit-cycle flapping

We consider a POD and DMD analysis of flapping with $Re = 500$, $M_\rho = 0.1$, and $K_B = 0.0001$, for which the system enters limit-cycle behavior (Connell and Yue, 2007). For these parameters, $R_\lambda = 1578.8$ and $R_G = 355.06$. Fig. 1 shows the transverse displacement of the trailing edge of the flag as a function of time along with the corresponding power spectral density. The figure also shows a phase portrait of transverse velocity versus transverse displacement, which exhibits a periodic orbit consistent with the observed limit-cycle behavior. Our analysis is performed after the transient region, once the system enters periodic behavior of fixed amplitude and frequency (beginning at $t \approx 20$ in Fig. 1). Fig. 2 shows contours of vorticity at four snapshots in time during a period of flapping in the limit cycle regime. Snapshots were obtained over the range $t \in [20, 40]$ in increments of $\Delta t = 0.05$.

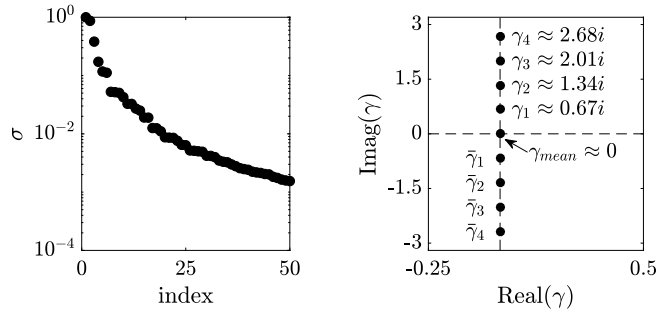


Fig. 3. POD singular values σ normalized by σ_1 (left) and DMD eigenvalues γ (right) for limit-cycle flapping of a conventional flag with $Re = 500$, $M_\rho = 0.1$, $K_B = 0.0001$.

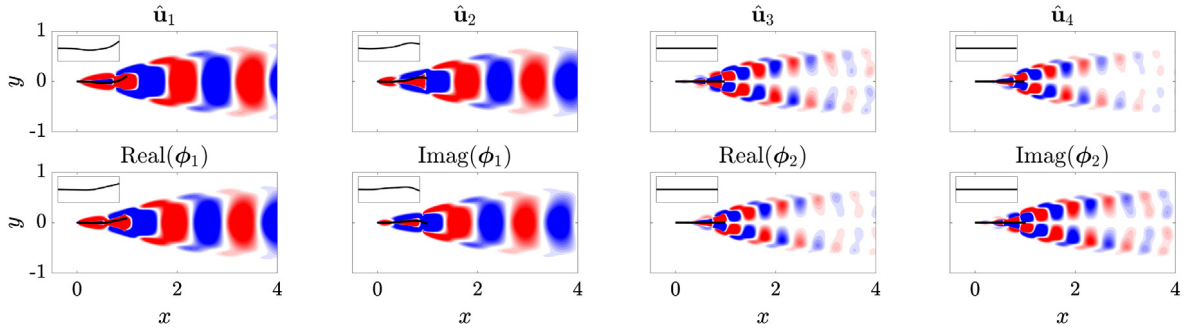


Fig. 4. Leading POD (top row) and DMD (bottom row) modes for the limit-cycle conventional-flag problem.

Fig. 3 shows the singular values σ from POD along with the DMD eigenvalues γ of largest growth rate (real part). The four leading POD modes (which represent approximately 85% of the total system energy) are shown in the top row of Fig. 4. Apart from the mode corresponding to the temporal mean, DMD modes typically come in complex conjugate pairs (e.g., the two leading modes are $\phi_1, \bar{\phi}_1$). We show in the bottom row of Fig. 4 the real and imaginary parts of ϕ_1 and ϕ_2 (the mode corresponding to the temporal mean is not pictured). The POD and DMD modes are nearly identical since this system is characterized by a specific frequency (c.f., Fig. 1). The energetically optimal modes are therefore driving behavior at this dominant frequency and its harmonics. The flag behavior is conveyed through the leading two POD modes (leading complex-conjugate pair of DMD modes): these modes represent phase-shifted flapping at the dominant frequency to create the traveling-wave behavior that the flag undergoes for these parameters (Connell and Yue, 2007). The two leading POD modes (leading complex-conjugate pair of DMD modes) also demonstrate the creation and advection of vortices associated with flapping. Subsequent modes are not associated with flag flapping (the flag mode in the insert is undeformed), and instead describe the higher-harmonic response of the fluid to this dominant flapping motion.

3.2. Route to chaotic flapping

We investigate the route to chaotic flapping here by choosing $M_\rho = 0.25$ (note that the increase in mass ratio does not affect R_λ or R_G). The trailing-edge displacement and corresponding spectral density for this regime are presented in Fig. 5. The figure also shows a phase portrait of the transverse velocity versus transverse displacement, which exhibits significant deviations from the periodic orbit seen in Fig. 1. Fig. 6 provides snapshots of the system over $t \in [28.6, 30.2]$. To demonstrate mathematically that this behavior is chaotic, we compute the Lyapunov exponent of the system using the time-delay method of Wolf et al. (1985) (this approach was also used by Connell and Yue, 2007 to identify chaotic flapping). The method produces an approximation of the distance in time, $d(t)$, of two trajectories starting close to one another at an initial time t^* . The evolution of this distance is written as $d(t) = d(t^*)e^{\alpha(t-t^*)}$, where α is the Lyapunov exponent that represents the departure or convergence of the two trajectories. A zero value of α corresponds to a stationary state where the system is in limit cycle behavior; a positive value of α corresponds to divergence of the two trajectories, and thus to chaotic flapping. Using this method, α was found to be 0.01 for the limit-cycle case of Section 3.1, and 0.2 for the chaotic flapping case of the present section. The relatively small positive exponent associated with the chaotic case is reflective of the fact that the physical parameters are near the critical value for the breakdown of limit cycle behavior – increasing the mass ratio to $M_\rho = 0.3$ leads to a Lyapunov exponent that is greater than one. The present case near the bifurcation is chosen to investigate the mechanism triggering chaos.

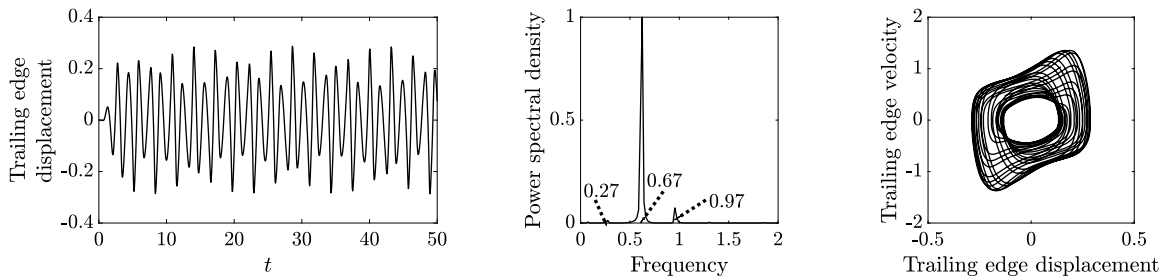


Fig. 5. For chaotic flapping with $Re = 500$, $M_\rho = 0.25$, and $K_B = 0.0001$: transverse displacement (left) and spectral density (middle) of the transverse motion of the trailing edge; (right) phase portrait of the transverse velocity versus the transverse displacement of the trailing edge.

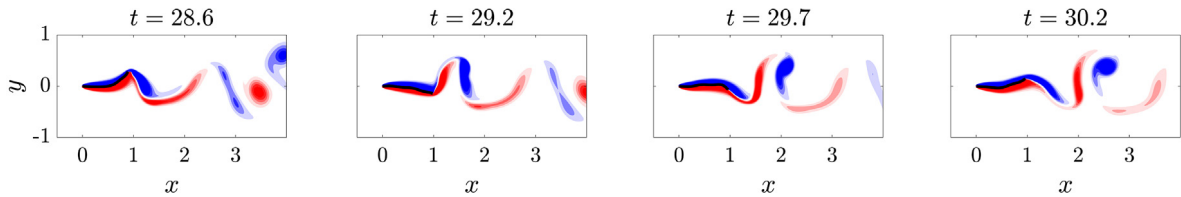


Fig. 6. Snapshots for a flag in chaotic flapping with $Re = 500$, $M_\rho = 0.25$, $K_B = 0.0001$. Snapshots are in roughly evenly spaced increments between the large ($t = 28.6$) and small ($t = 30.2$) positive peaks. Contours are of vorticity, in 18 increments from -5 to 5 .

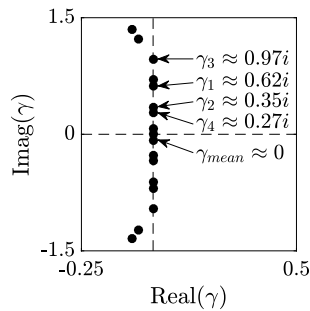


Fig. 7. DMD eigenvalues γ for chaotic flapping of a conventional flag with $Re = 500$, $M_\rho = 0.25$, $K_B = 0.0001$.

Note from the middle plot in Fig. 5 that there are multiple frequencies present at non-integer harmonics of the dominant frequency. These non-integer frequencies associated with the onset of chaos were first observed by Connell and Yue (2007), and the mechanism that introduces them remains unexplained. Using DMD within our FSI framework, we propose that chaotic flapping is instigated by the increase in flapping amplitude associated with the increased mass ratio. This increase in amplitude leads the flag to become sufficiently bluff to the flow at its peak deflection that a bluff-body wake instability arises and interacts triadically with the dominant flapping behavior to produce the subdominant flapping frequencies observed in Fig. 5. DMD is selected here to isolate behavior at distinct frequencies. This can be done in a POD context using spectral POD (SPOD) (Towne et al., 2018), and future work could compare the results between DMD and SPOD.

The DMD eigenvalues γ and four leading modes ϕ (omitting the mode associated with the mean) for the chaotic case of $M_\rho = 0.25$ are shown in Figs. 7 and 8. The dominant and non-integer harmonic frequencies from the spectral density plot of Fig. 5 manifest themselves in DMD modes ϕ_1 , ϕ_3 , and ϕ_4 (see the corresponding eigenvalues in Fig. 7). Note that despite the significant change in behavior from the limit-cycle regime, ϕ_1 remains largely unchanged. Yet, due to the increased system complexity, flapping is no longer conveyed entirely through the first mode, and both ϕ_3 and ϕ_4 are associated with flapping motion and a correlated set of flow features.

By contrast, ϕ_2 is not associated with flapping (the flag mode in the insert is undeformed). This is consistent with the absence of the γ_2 frequency in the spectral density plot of Fig. 5. Thus, the mode represents a response of the fluid to the dominant flapping motion. The pronounced shear layers at the top and bottom peak displacement and the corresponding wake vortices are reflective of a bluff-body vortex-shedding mode that appears because of the increased flapping amplitude compared with the limit-cycle case. Note also that when written as a Strouhal number (using the projected length of the maximum peak-to-peak-amplitude as the normalizing length scale), the modal frequency agrees with the classical 0.2 Strouhal scaling (Roshko, 1954) (i.e., $0.35 \times 0.5 \approx 0.18$). To provide further evidence that this mode corresponds to bluff-body

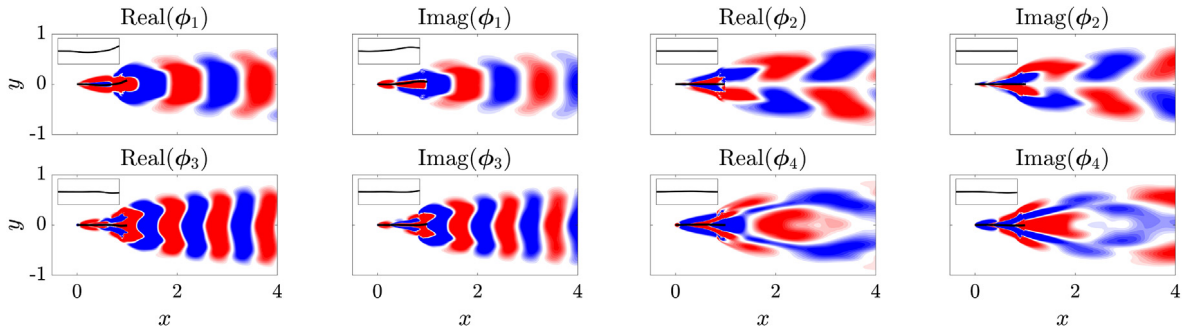


Fig. 8. Leading DMD modes for chaotic flapping of a conventional flag with $Re = 500$, $M_\rho = 0.25$, $K_B = 0.0001$.

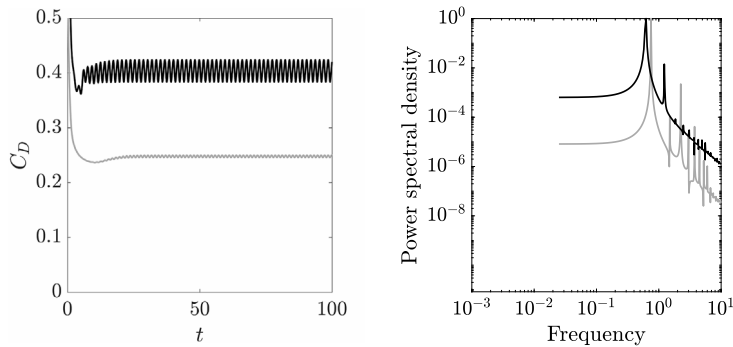


Fig. 9. Coefficient of drag, C_D , (left) and spectral density (right) of the rigid, stationary flags with $Re = 500$. —: rigid flag fixed at the peak deflection position associated with limit-cycle flapping. - - -: rigid flag fixed at the peak deflection position associated with the chaotic regime.

vortex shedding, we present results from simulations of flow past a rigid flag fixed in the peak deflection position for both the limit-cycle and chaotic cases. Fixing the flag at the peak deflection position of the different flapping regimes allows us to probe whether a wake stability should be expected in each regime.

For limit-cycle flapping, we show in Fig. 9 that for the associated rigid-body simulations, vortex shedding is negligible, with oscillations in the coefficient of drag having a peak-to-peak departure from the mean value of less than 1%. By contrast, for the rigid-body simulations corresponding to the chaotic case, the oscillations in the drag have a peak-to-peak departure from the mean value of over 12%, which demonstrates the potential for a larger-amplitude wake-response in the corresponding FSI simulations. Note from the power spectral density plot in Fig. 9 that the vortex shedding frequency is roughly double γ_2 – the frequency of the vortex shedding mode, ϕ_2 . This factor of two can be accounted for by observing that for ϕ_2 , the vortices are shed above and below the centerline (commensurate with the fact that in the FSI simulations, oppositely-signed vortices are shed at the top and bottom part of the cycle, respectively). That is, a new vortex above (below) the centerline is shed at a frequency of γ_2 , but a vortex is shed from either above or below the centerline at a frequency of $2\gamma_2$. The dominant frequencies in figure 9 bound $2\gamma_2$ from above and below, which suggests that there is an effective bluff body the flow experiences in chaotic flapping whose peak deflection is intermediate to these two extremal cases. These rigid body simulations suggest that in the transition to chaotic flapping, the flapping amplitude increases beyond a threshold value for which bluff-body vortex shedding ensues and interacts with the primary flapping behavior.

This bluff-body mode is key to understanding the sub-dominant flapping behavior of the flag: the sub-dominant frequencies seen in Fig. 5 arise as triadic combinations of the frequencies of the dominant flapping mode and the bluff-body mode; *i.e.*, $\gamma_3 = \gamma_1 + \gamma_2$ and $\gamma_4 = \gamma_1 - \gamma_2$. These triadic interactions are necessitated by the quadratic nonlinearity of the advective term in the Navier–Stokes equations.

This chaotic flapping case highlights the utility of this combined fluid–structure formulation. The coupled fluid–structure modes reveal that ϕ_1 , ϕ_3 , and ϕ_4 are associated with correlated fluid–structure behavior but ϕ_2 contains only a response in the fluid. This provides an indication that the latter mode is associated with a flow instability. One might be able to deduce this from comparing fluid-only and structure-only modal decompositions, but the built-in fluid–structure correlations of our proposed decomposition removes the need to guess at connections (or lack thereof) between the fluid and structure.

4. Conclusions

We presented a formulation for performing data analysis on FSI problems that accounts for both the fluid and the structure. We designed this formulation to be compatible with the manner in which data is typically obtained for experiments

and nonconforming mesh simulations. As part of this framework, we defined a physically meaningful norm for FSI systems. We considered POD and DMD because of their widespread use, but extensions to other methods are straightforward.

Our formulation was first applied to limit-cycle flag flapping. Because of the dominant frequency associated with this limit-cycle behavior, both POD and DMD give similar decompositions. The leading two POD modes (leading complex-conjugate pair of DMD modes) convey both the flapping information of the flag and the dominant vortical structures associated with this motion. Subsequent modes describe harmonic responses in the fluid to the flapping described in the leading modes.

Next, the physical mechanism driving chaotic flapping was clarified. [Connell and Yue \(2007\)](#) identified that the transition from limit-cycle flapping to chaotic flapping coincides with the appearance of a new flapping frequency near the 3/2 harmonic of the dominant flapping frequency. We identified the mechanism driving this non-integer harmonic through a DMD analysis. We first demonstrated that at the onset of chaos, the flag becomes sufficiently bluff at its peak deflection to initiate a bluff-body wake instability. This is in contrast to limit-cycle flapping, where flapping amplitudes are smaller and this bluff-body instability is not instigated. The associated shedding frequency of this new behavior coincides with the Strouhal scaling of 0.2 common to bluff-body flows ([Roshko, 1954](#)). Moreover, we demonstrated that this bluff-body mode combines triadically with the dominant flapping behavior to produce the observed flapping near the 3/2 harmonic (and the other sub-dominant flapping frequencies).

Last, we note that many reduced-order models of FSI systems are formed by performing a decomposition of the fluid and coupling this reduced representation to the full governing equations of the structure. It is possible that the proposed fluid–structure decomposition technique could lead to more efficient low-order models, which provides avenues for future investigations.

Acknowledgments

Andres Goza and Tim Colonius acknowledge funding through the Robert Bosch LLC through Bosch Energy Network Grant number 07.23.CS.15 and through the AFOSR (grant number FA9550-14-1-0328). Andres Goza is also grateful to Dr. Scott Dawson for his thoughtful comments on an early version of the manuscript.

Appendix. Construction of \mathbf{W} for flag flapping

We discuss here the creation of \mathbf{W} for the flag flapping problem considered in Section 3. To do this, we first note our use of the dimensionless parameters from (7) in place of the dimensional parameters presented in Section 2.1. The first and third sub-blocks are fully specified by defining $\beta_f = \Delta x \sqrt{1/2}$, $\beta_s = \sqrt{\Delta \tilde{x}(h/L)} \sqrt{M_\rho}$ (where h is the flag thickness and L is the flag length). The term $\sqrt{\Delta \tilde{x}(h/L)}$ arises from the fact that the integral over Γ may be written as a double integral, with one integration occurring along the flag's length (corresponding to the $\Delta \tilde{x}$ scaling), and the other performed along the cross section. The result of this latter integral is the flag thickness (which in this case is written nondimensionally through a scaling with L), as all quantities are taken to be constant at a fixed value of \tilde{x} .

We now specify \mathbf{L} using the bending strain provided in (8), which is valid even in the presence of geometric nonlinearity. For boundary conditions, the flag is pinned at its leading edge, leading to

$$\chi(\tilde{x} = 0) = 0, \eta(\tilde{x} = 0) = 0. \quad (\text{A.1})$$

For non-boundary points, a second-order central difference scheme is employed to approximate the first derivatives, except at the trailing edge where a one-sided derivative is necessary. We thus write \mathbf{L} as the block diagonal matrix

$$\mathbf{L} = \begin{bmatrix} \mathbf{L}^\chi & \\ & \mathbf{L}^\eta \end{bmatrix} \quad (\text{A.2})$$

with

$$\mathbf{L}^\chi (\in \mathbb{R}^{n_s \times n_s}) = \frac{\beta_1}{\Delta \tilde{x}} \begin{bmatrix} \Delta \tilde{x} / \beta_1 & & & & & \\ -1/2 & 0 & 1/2 & & & \\ & \ddots & \ddots & \ddots & & \\ & & -1/2 & 0 & 1/2 & \\ & & & -1 & 1 & \end{bmatrix} \quad (\text{A.3})$$

where $\beta_1 = \sqrt{1/2(R_\lambda/2 + R_G)}$, and

$$\mathbf{L}^\eta (\in \mathbb{R}^{n_s \times n_s}) = \frac{\beta_2}{\Delta \tilde{x}} \begin{bmatrix} \Delta \tilde{x} / \beta_2 & & & & & \\ -1/2 & 0 & 1/2 & & & \\ & \ddots & \ddots & \ddots & & \\ & & -1/2 & 0 & 1/2 & \\ & & & -1 & 1 & \end{bmatrix} \quad (\text{A.4})$$

where $\beta_2 = \sqrt{R_G/4}$. Defining \mathbf{L} in this way, and letting $\boldsymbol{\tau} = [\boldsymbol{\chi}, \boldsymbol{\eta}]^T$, $\boldsymbol{\tau}^T \mathbf{L} \boldsymbol{\tau}$ is an approximation of κ .

To complete our construction of \mathbf{W} , we set $\beta_\kappa = \sqrt{\Delta\bar{x}(h/L)}$. From this definition of \mathbf{W} , and defining $\mathbf{q} = [\mathbf{u}, \mathbf{v}, \chi, \eta, \xi, \zeta]^T$, $\mathbf{q}^T \mathbf{W}^T \mathbf{W} \mathbf{q}$ is an approximation of (1), as desired. Note that \mathbf{L} (and therefore \mathbf{W}) is not symmetric, but the \mathbf{W} -norm satisfies the necessary definitions of a norm nonetheless, since it is formulated in terms of the symmetric positive definite matrix $\mathbf{W}^T \mathbf{W}$.

References

- Alben, S., Shelley, M.J., 2008. Flapping states of a flag in an inviscid fluid: bistability and the transition to chaos. *Phys. Rev. Lett.* 100 (7).
- Bagheri, S., 2013. Koopman-mode decomposition of the cylinder wake. *J. Fluid Mech.* 726, 596–623.
- Bathe, K.-J., 2014. *Finite Element Procedures*. Bathe, Klaus-Jürgen.
- Berkooz, G., Holmes, P., Lumley, J.L., 1993. The proper orthogonal decomposition in the analysis of turbulent flows. *Annu. Rev. Fluid Mech.* 25 (1), 359–575.
- Blanchard, A., Bergman, L.A., Vakakis, A.F., 2017. Targeted energy transfer in laminar vortex-induced vibration of a sprung cylinder with a nonlinear dissipative rotator. *Physica D* 350, 26–44.
- Bozkurttas, M., Mittal, R., Dong, H., Lauder, G., Madden, P., 2009. Low-dimensional models and performance scaling of a highly deformable fish pectoral fin. *J. Fluid Mech.* 631, 311–342.
- Cesur, A., Carlsson, C., Feymark, A., Fuchs, L., Revstedt, J., 2014. Analysis of the wake dynamics of stiff and flexible cantilever beams using POD and DMD. *Comput. & Fluids* 101, 27–41.
- Chen, K.K., Tu, J.H., Rowley, C.W., 2012. Variants of dynamic mode decomposition: boundary condition, Koopman, and Fourier analyses. *J. Nonlinear Sci.* 22 (6), 887–915.
- Colonius, T., Taira, K., 2008. A fast immersed boundary method using a nullspace approach and multi-domain far-field boundary conditions. *Comput. Methods Appl. Mech. Engrg.* 197 (25), 2131–2146.
- Connell, B.S., Yue, D.K., 2007. Flapping dynamics of a flag in a uniform stream. *J. Fluid Mech.* 581, 33–67.
- Dowell, E.H., Hall, K.C., 2001. Modeling of fluid-structure interaction. *Annu. Rev. Fluid Mech.* 33 (1), 445–490.
- Goza, A., Colonius, T., 2017. A strongly-coupled immersed-boundary formulation for thin elastic structures. *J. Comput. Phys.* 336, 401–411.
- Kim, D., Cossé, J., Cerdeira, C.H., Gharib, M., 2013. Flapping dynamics of an inverted flag. *J. Fluid Mech.* 736.
- Kutz, J.N., Brunton, S.L., Brunton, B.W., Proctor, J.L., 2016. *Dynamic Mode Decomposition: Data-Driven Modeling of Complex Systems*. SIAM.
- Mezić, I., 2013. Analysis of fluid flows via spectral properties of the Koopman operator. *Annu. Rev. Fluid Mech.* 45, 357–378.
- Michelin, S., Smith, S.G.L., Glover, B.J., 2008. Vortex shedding model of a flapping flag. *J. Fluid Mech.* 617, 1–10.
- Roshko, A., 1954. On the Drag and Shedding Frequency of Two-Dimensional Bluff Bodies, Tech. Rep., National Advisory Committee for Aeronautics, Washington, DC, United States.
- Rowley, C.W., Mezić, I., Bagheri, S., Schlatter, P., Henningson, D.S., 2009. Spectral analysis of nonlinear flows. *J. Fluid Mech.* 641, 115–127.
- Schmid, P., 2010. Dynamic mode decomposition of numerical and experimental data. *J. Fluid Mech.* 656, 5–28.
- Sirovich, L., Kirby, M., 1987. Low-dimensional procedure for the characterization of human faces. *J. Opt. Soc. Am. A* 4 (3), 519–524.
- Tangorra, J.L., Lauder, G.V., Hunter, I.W., Mittal, R., Madden, P.G., Bozkurttas, M., 2010. The effect of fin ray flexural rigidity on the propulsive forces generated by a biorobotic fish pectoral fin. *J. Exp. Biol.* 213 (23), 4043–4054.
- Towne, A., Schmidt, O.T., Colonius, T., 2018. Spectral proper orthogonal decomposition and its relationship to dynamic mode decomposition and resolvent analysis. *J. Fluid Mech.* 847, 821–867.
- Tu, J.H., Rowley, C.W., Luchtenburg, D.M., Brunton, S.L., Kutz, J.N., 2014. On dynamic mode decomposition: theory and applications. *J. Comput. Dyn.* 1, 391–421.
- Wolf, A., Swift, J.B., Swinney, H.L., Vastano, J.A., 1985. Determining lyapunov exponents from a time series. *Physica D* 16 (3), 285–317.